Journal of Materials Science & Technology xxx (2020) xxx–xxx

Contents lists available at ScienceDirect

Journal of Materials Science & Technology

journal homepage: www.jmst.org

Research Article

Superparamagnetic iron oxide nanoparticles assembled magnetic nanobubbles and their application for neural stem cells labeling

Jing Li, Zhenqiang Feng, Ning Gu*, Fang Yang*

State Key Laboratory of Bioelectronics, Jiangsu Key Laboratory for Biomaterials and Devices, School of Biological Sciences and Medical Engineering, Southeast University, Nanjing 210096, China

ARTICLE INFO

Article history:
Received 15 December 2019
Received in revised form 2 February 2020
Accepted 17 February 2020
Available online xxx

Keywords:
Nanobubbles
Superparamagnetic nanoparticles
Self-assembly
Neural stem cells
Ultrasonic exposure

ABSTRACT

Micro/nanobubbles for use as ultrasound contrast agents have been fabricated with different shell materials. When various biomedical nanoparticles have been embedded in the shells of bubbles, the composite structures have shown promising applications in multi-modal imaging, drug/gene delivery, and biomedical sensing. In this study, we developed a new gas-liquid interface self-assembly method to prepare magnetic nanobubbles embedded with superparamagnetic iron oxide nanoparticles (SPIONs). The diameter of the generated assembled nanobubbles was 227.40 ± 87.21 nm with a good polydispersity index (PDI) of 0.29. Under the condition of 150 compression cycles, the nanobubble concentration could reach about 6.12×10^9/mL. Transmission electron microscopy (TEM) and scanning electronic microscopy (SEM) demonstrated that the assembled nanobubbles had a hollow gas core with SPIONs adsorbed on the surface. Ultrasound (US) imaging and magnetic resonance imaging (MRI) experiments indicated that the assembled magnetic nanobubbles exhibited good US and MR contrast capabilities. Moreover, the assembled magnetic nanobubbles were used to label neural stem cells under ultrasound exposure. After 40 s US exposure, the magnetic nanobubbles could be delivered into cells with 2.80 pg Fe per cell, which could be observed in the intracellular endosome by TEM. Compared with common incubation methods, the ultrasound exposure method did not introduce the potential cytotoxicity of transfection reagents and the efficiency was about twice as high as the efficiency of incubation. Therefore, the assembled magnetic nanobubbles prepared through the pressure-driven gas-liquid interface assembly approach could be a potential US/MRI dual model imaging nanocarrier for regenerative applications.

1. Introduction

In the last few decades, micro/nanobubbles have been found to be useful in a variety of biomedical applications such as targeted drug delivery and ultrasound contrast enhancement [1–4]. Compared with microbubbles with a diameter above 1 μm, nanobubbles with a diameter below 700 nm possess several special properties, including high stability, large surface area, and quite strong adsorption capacity [5–8]. Gas core is an important structural component of micro/nanobubbles. The second or third generation of ultrasound contrast agents developed in recent years mainly use macromolecular inert gases of low dispersion coefficient and low blood solubility, such as perfluorocarbon (C_3F_8) or sulfur hexafluoride (SF_6) [9,10]. The microbubbles filled with SF_6 (SonoVue®) are one of the representative ones. They have been commonly used in clinical applications and research field [11].

In recent years, more and more researches have focused on coating different materials on the surface of bubbles. The micro/nanobubble modified with proteins and nanoparticles on the shell may not only possess much better stability with significantly improved resistance to pressure and mechanical variations but also exhibit greater versatility due to the presence of functional agents [12–14]. These materials can be embedded on shells of micro/nanobubbles through a variety of methods, mainly including biochemical conjugation [15–17] and physical methods, such as electrostatic interaction [18,19], microfluidic devices [20], and sonication [14]. The binding force degree of chemical coupling is stronger than that of the physical effect [16,21]. Physical methods such as microfluidic devices can produce uniform bubbles and predetermine the size of the microbubbles [22,23]. However, existing methods require additional carrier layers such as polymers and

* Corresponding authors.
E-mail addresses: guning@seu.edu.cn (N. Gu), yangfang2080@seu.edu.cn (F. Yang).

https://doi.org/10.1016/j.jmst.2020.02.045
1005-0302/

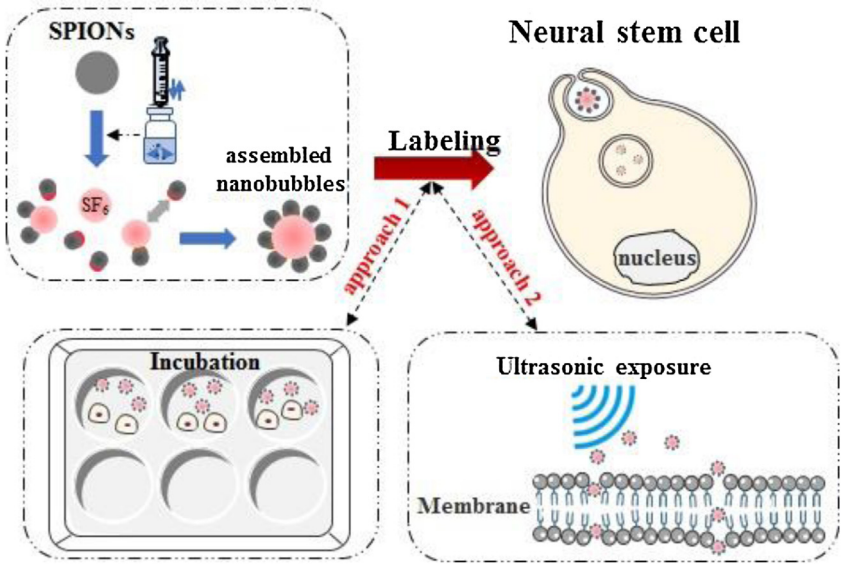

Fig. 1. Schematics of SPIONs assembled magnetic nanobubbles and their application for neural stem cell labeling with different methods. SPIONs: Superparagmagnetic iron oxide nanoparticles.

oil layers or complex conjugation strategies that involve multiple processing steps and are time consuming [24,25]. Moreover, the shells of the presently available micro/nanobubbles are often made of polymers or phospholipids with the introduction of organic solvents.

Nanoparticles, especially superparamagnetic iron oxide nanoparticles (SPIONs), as the membrane shell material have drawn great attention due to their unique physical, chemical, and biological properties. SPIONs have been incorporated into micro/nanobubble shells, and the resulting composite micro/nanobubble structures have been applied to enhance multimode imaging and drug delivery. Yang et al. [26] and Duan et al. [27] developed microbubbles with SPIONs embedded in polymer shells for ultrasound (US)/magnetic resonance imaging (MRI) dual contrast imaging. Park et al. [28] produced stable microbubbles that can attach different types of nanoparticles, including Fe_3O_4 or Au, to their surface for US/MRI or photoacoustic imaging contrast enhancement. Ultrasmall-SPIONs were embedded in the wall of poly (butyl cyanoacrylate)-based microbubbles, which allowed the blood-brain barrier to be monitored [29]. Some other studies have also demonstrated that incorporating nanoparticles into phospholipid-coated microbubbles increases the efficiency of gene delivery [30,31]. Nanobubbles loaded with SPIONs and/or antibody-drugs have been studied for tri-modal biological imaging and targeted therapy [12,32]. All these studies have shown that nanoparticle-loaded micro/nanobubbles could be successfully used for bio-separation, magnetic drug delivery, and MRI contrast enhancement for a specific organ and the long-term tracking of cellular fate in vivo [33,34].

Stem cell-based therapy is emerging as a promising alternative therapeutic strategy to improve or treat disease. Neural stem cells (NSCs), which are characterized by high self-renewal and multidifferentiation, may be a possible strategy for naturally homing to diseased regions and replacing cell loss to treat conditions such as stroke, spinal cord injury, Alzheimer's disease, or amyotrophic lateral sclerosis [35–38]. However, tracking the accumulation of stem cells in sites of interest and their fate in vivo is a prerequisite for the use of stem cell therapy. Previous studies have shown that microbubbles exhibit great potential for stem cell tracking and therapy. Microbubbles or nanobubbles as a carrier for transferring growth factors were successfully used to label stem cells and were shown to have good imaging ability and even feasibility to treat disease in vivo [39,40]. However, few studies have reported on nanobubbles for labeling stem cells. Studies using SPIONs as the MRI contrast agents in stem cell labeling or tracking have increased exponentially in recent years [41]. The most commonly-used labeling approach is "simple incubation" [42]. However, this method takes several hours for incubation, and one researcher revealed that transfection reagents may increase the cell apoptosis rate [43].

In this study, as shown in Fig. 1, we developed a novel structure of self-assembled SPION-embedded nanobubbles without any polymer or phospholipid shells and without the use of organic solvents. The characterization and properties of the assembled magnetic nanobubbles were investigated in detail, and a possible generation mechanism was proposed. More importantly, the preliminarily validated labeling efficiency of NSCs under ultrasonic exposure was measured quantitatively, and the intracellular distribution of magnetic nanobubbles was characterized.

2. Experimental

2.1. Materials

Ultrapure water with the conductivity of 18.25 Ω/cm was prepared with a deionizing water purification system (ULPURE UPH-IV-10 T, China). The gas used in the experiment was SF_6 with a purity of 99.99 % purchased from Anhui Qiangyuan Gas Co., Ltd (Wuhu, China). Glass vials (4 mL) with open screw caps containing Teflon-covered silicon rubber septa and a 5 mL syringe fitted with a 22 G needle (KDL, Shanghai, China) were used to produce samples. Finally, γ-Fe_2O_3 superparamagnetic iron oxide nanoparticles (SPIONs, mean TEM diameter: 7 nm; mean hydrodynamic diameter: about 30 nm; concentration: 5.67 mg/mL) were synthesized and modified with poly-glucose sorbitol carboxymethyl ether (PSC), which was provided by the Jiangsu Key Laboratory for Biomaterials and Devices (Nanjing, China) [44].

2.2. Synthesis of SPIONs assembled nanobubbles

Assembled nanobubbles were prepared by a repeated compression method similar to the process described in our previous study [6]. Briefly, 2 mL of deionized (DI) water and SPIONs with different concentrations were added to 4 mL glass vials. The air layer in the upper part of the vial was replaced with SF_6 gas, and then the vial

was sealed. After that, a 5 mL syringe containing 3 mL of SF_6 gas with the needle was inserted into the vial. The tip of the needle was always kept below the water surface during the process. The whole process of piston up and down movements was recorded as one compression cycle. The moving speed of piston (10, 16, 22, 26, 28, 30 mm/s) and number of compression cycles (30, 70, 100, 150) as well as the concentration of SPIONs (5.67, 8.50, 11.34, 19.85, 28.35 μg/mL) added to the vial were measured to acquire the optimal conditions for assembly. The operation was conducted at room temperature (25 °C).

2.3. Structural and functional characterization of assembled nanobubbles

The size distribution and Zeta potential of assembled nanobubbles were measured using a NanoSizer (Zeta-Sizer, Malvern Instruments, United Kingdom) at a 90° scattering angle. The concentration measurement of assembled nanobubbles in solution was performed by a nanoparticle tracking analysis (NTA) instrument (NanoSight, NS300, Malvern Instruments). A transmission electron microscope (TEM, JEM-2100, Japan) and a scanning electron microscope (SEM, Ultra Plus, Zeiss, Germany) were used to characterize the morphology of assembled nanobubbles. Inductively Coupled Plasma Optical Emission Spectrometer (ICP-OES, Optima 8000, PerkinElmer, USA) was used to determine the amount of SPIONs on nanobubbles, which was indirectly compared with the nanoparticle solution through calculating the iron concentration.

MRI experiments of assembled nanobubbles were carried out on a 7.0 T MRI scanner (Biospec 7 T/20 USR, Bruker, Germany). The detailed parameters for T_2 imaging were set as follows: field of view (FOV) = 33 mm × 80 mm, flip angle (FA) = 90°, slice thickness = 1.50 mm, echo time (TE) = 36 ms, repetition time (TR) = 3000 ms. The gray value was measured in regions of interests (ROIs) in the sample area as the signal intensity.

Ultrasound imaging was performed on a high-resolution microimaging system (VisualSonics Vevo 2100, Canada) with the transducer at 18 MHz of a static state using both B-mode and contrast mode. The imaging settings for the system were center frequency of 18 MHz, intensity power of 4 %, and contrast gain of 35 dB. A grayscale mapping function was used to calibrate the ultrasound video intensity.

2.4. Neural stem cell culture and label in vitro

Primary NSCs were extracted from the hippocampi of 14 days-old fetal rats according to established protocols [45] in accordance with the Guidelines for Animal Care and Use established by the Medical School of Southeast University's Institutional Animal Care and Use Committee. Pregnant rats were sacrificed, and neural stem cells were isolated from the hippocampi of fetuses by microdissection and dissociation using 0.25 % trypsin-EDTA (Gibco by Life Technologies, USA). Cells were collected and re-suspended in serum-free DMEM/F12 medium (Gibco) supplemented with 2 % B27 (Gibco), 20 ng/mL Recombinant Rat epidermal growth factor (EGF, PeproTech, USA), 20 ng/mL Recombinant Rat basic fibroblast growth factor (bFGF, PeproTech), 2 nM L-glutamine (Aladdin, China), and 2 μg/mL Heparin sodium salt (Aladdin). This suspension was incubated under the conditions of 37 °C and 5 % CO_2. Fresh medium was changed every three days, and cells were dissociated with Accutase Dissociation Reagent (STEMCELL Technologies, Canada) until cell neurospheres reached a diameter greater than 500 μm.

For stem cell labeling, the ultrasound exposure system described in our earlier publication was used in this study [46]. Briefly, the 1 MHz focused 30 mm-diameter single-element transducer was positioned in a water tank and connected to a waveform generator (33250A Agilent Technologies, USA) and radio frequency (RF) power amplifier (75A250, Amplifier Research, USA). The concentration ratio of assembled nanobubbles to cells was about 10:1. After mixing, the cell suspension was placed into a plastic tube of 15 mm diameter and 75 mm length with a sound-transparent polymer-membrane bottom. The optimum acoustic pressure for labeling was measured by comparing cell viability via the CCK-8 assay (Cell Counting Kit-8, Beyotime, China). For measuring cell uptake of assembled nanobubbles, Prussian blue staining assay and ICP-OES quantitative analysis were performed after ultrasound exposure. For further analysis, the labeled cells were detached and fixed overnight with 2.50 % glutaraldehyde in 1 × phosphate buffer solution (PBS, pH 7.40) at 4 °C. The samples were then postfixed in 1 % osmium tetroxide, dehydrated in ethanol, and embedded in epon (Sigma-Aldrich, MO, USA). Ultrathin slices (60–80 nm) were stained with uranyl acetate and lead citrate and imaged by TEM (JEM-2100, Japan).

2.5. Statistical analysis

Statistical calculations were performed in GraphPad Prism Version 7.0, and all values were presented as mean ± SD of more than three independent experiments. Comparisons were conducted using one-way analysis of variance (ANOVA) followed by the *t*-test. Values of $^{*}p < 0.05$ and $^{**}p < 0.01$ were considered statistically significant. All reported p values were two-tailed.

3. Results and discussion

3.1. Synthesis and characterization of assembled nanobubbles

Assembled nanobubbles were prepared by repeated compression to cause the nanoparticles to be absorbed on the surfaces of the nanobubbles. The parameters of compression speed and number of compression cycles were set in this study based on our previous study to ensure the generation of nanobubbles and also to verify the feasibility of adding SPIONs [6]. By measuring the size distribution (Fig. 2(a1-1)) and analyzing the count rate of bubbles and the peak ratio of free SPIONs (Fig. 2(a1-2)) in different compression speeds, it was found that all sizes were distributed with two peaks (about 30 nm for free SPIONs and 200 nm for nanobubbles). Meanwhile, the peak ratio of free SPIONs decreased with increasing the rate of bubbles, and it may reveal that with increasing the speed, more and more free SPIONs in solution adsorbed on nanobubbles. Similarly, the results of samples with different compression cycles showed that the size distributed in 30 nm disappeared as the compression cycles approached 150 (Fig. 2(a2-1)). And the further studies on the count rate of bubbles and on the peak ratio of free SPIONs indicated that as the time increased, the peak ratio decreased with increasing the count of bubbles (Fig. 2(a2-2)) at the same compression speed (30 mm/s). Therefore, the compression speed of 30 mm/s and 150 compression cycles were used to measure the optimal concentration of SPIONs. The size distributions of samples in different concentrations of SPIONs revealed that the detectable free SPIONs (about 30 nm) remained in solution as the concentration increased (Fig. 2(a3-1)). Under the concentrations of 5.67 μg/mL and 8.50 μg/mL, a single peak was observed at about 200 nm, and the peak of ratio of free SPIONs did not appear, which may indicate that almost all SPIONs assembled on nanobubbles (Fig. 2(a3-1, 3-2)). When the concentration of SPIONs was 11.34 μg/mL, the peak ratio began to appear but was lower than the peak ratios under the concentrations of 19.85 and 28.35 μg/mL. These results suggested that the concentration of 11.34 μg/mL could be set for further studies to ensure enough SPIONs assemble on nanobubbles. Based on the above results, the following compression parameters were cho-

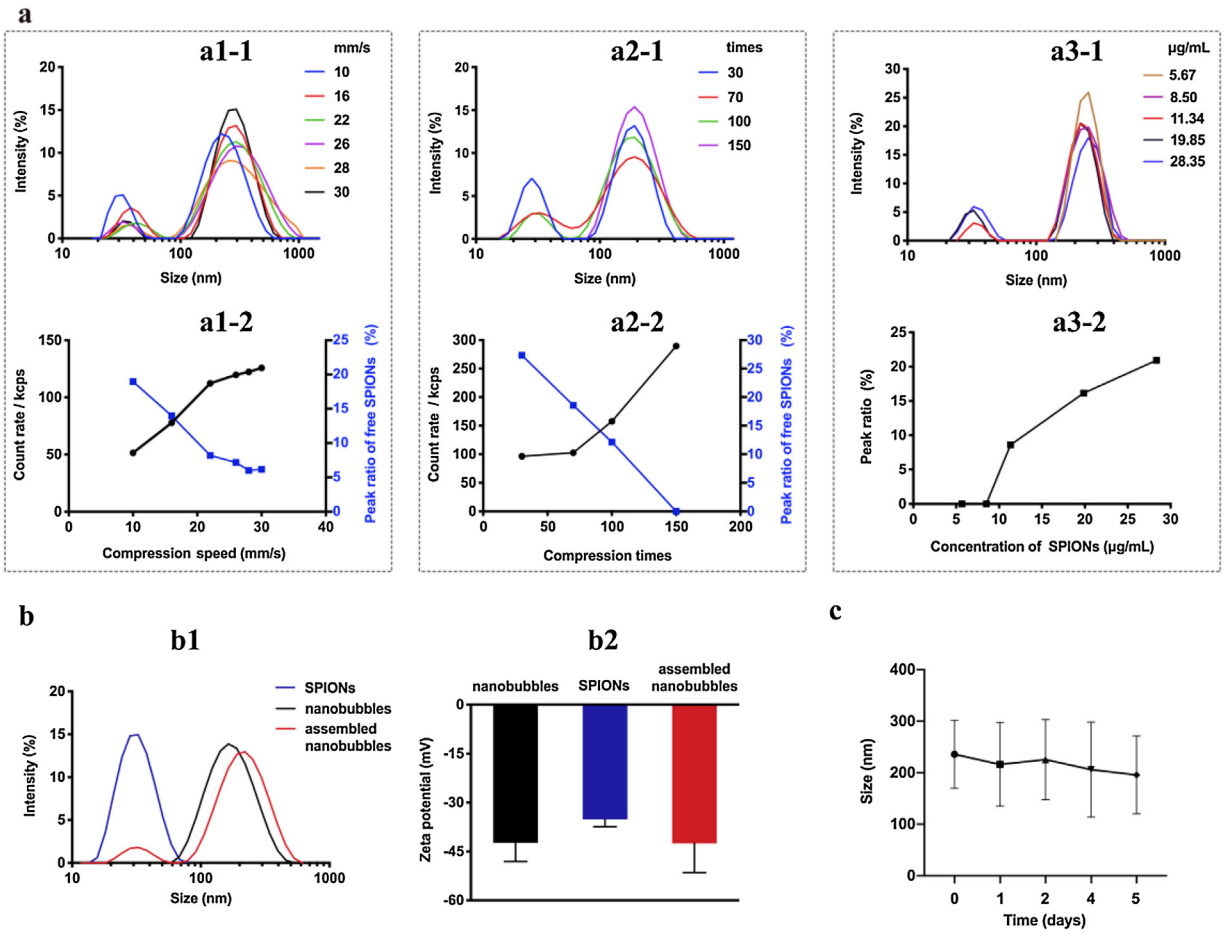

Fig. 2. Assembled parameters and characterization of assembled magnetic nanobubbles. (a) Effect of compression speed (a1-1) for size distribution; (a1-2) for count rate of bubbles and peak ratio of free SPIONs), compression cycles (a2-1) for size distribution; (a2-2) for count rate of bubbles and peak ratio of free SPIONs) and the concentration of SPIONs (a3-1) for size distribution; (a3-2) for peak ratio of free SPIONs) on assembled nanobubbles; (b) size distribution (b1) and zeta potential (b2) of nanobubbles, nanoparticles and assembled nanobubbles by NanoSizer. All bars represent mean ± SD, and three independent experiments (n = 3) were performed; (c) The stability of assembled magnetic nanobubbles at room temperature (25 °C).

sen for further studies: compression speed of 30.00 mm/s, cycles of 150, and concentration of SPIONs as 11.34 μg/mL.

The size and zeta potential of free nanobubbles, SPIONs, and assembled nanobubbles were all measured with the dynamic light scattering (DLS), and the first two were set as control groups to assess differences before and after assembly. Fig. 2(b1) verifies the size probability distribution function of the sample. For free nanobubbles, it shows single size distribution around 181 nm. And for assembles nanobubbles, there are two peaks. The intensity peak around 32 nm (32.68 ± 7.34 nm) was almost consistent with the SPIONs (31.01 ± 6.05 nm), which indicates the unassembled SPIONs in the solution. And the peak of about 230 nm (227.40 ± 87.21 nm) is fairly close to the size of the nanobubbles (182.00 ± 71.77 nm). The above results suggest that unassembled SPIONs were present in the assembled nanobubbles solution, and the small size difference between nanobubbles and assembled nanobubbles reveals the occurrence of the self-assembly process. The polydispersity indexes (PDIs) of all three materials including free nanobubbles, SPIONs and assembled nanobubbles were 0.19, 0.24, and 0.29, respectively, which indicates the uniform size of samples. The zeta potential had no significant difference among all these samples (Fig. 2(b2)).

Particle analysis using the NTA method was further performed to quantitatively investigate the concentrations of assembled nanobubbles in solution. The concentration of assembled nanobubbles with 150 cycles repeat compression at a speed of 30 mm/s could reach up to 6.12 × 10^9 particles/mL. The result shown in Fig. 2(c) further demontrates that the size of assembled nanobubbles at room temperature (25 °C) indicates no significant difference within 5 days, ranging from 235.90 ± 65.00 nm to 195.77 ± 75.30 nm after 5 days.

3.2. Morphological characterization of assembled nanobubbles

TEM and SEM images shown in Fig. 3(b, c) were used to observe the self-assembly structure of the sample. After the SPIONs with TEM diameter of 7 nm (Fig. 3(a)) were assembled on the gas-liquid interface, the TEM images of magnetic nanobubbles clearly exhibited that the nanoparticles were bonded on the surface of nanobubbles to form a regular circle structure. The TEM size of magnetic nanobubbles was about 150 nm, which is almost consistent with the size measured by DLS. Assembled structures are also shown in the SEM images (Fig. 3(c)). To further analyze the distribution of atomic percentage, especially for Fe, an assembly structure was randomly selected in the field of view, and the energy dispersive spectrometer (EDS) module of SEM was used. The results in Fig. 3(d) show that the Fe element was detected in samples with the mass percentage of 0.51 % and the atomic percentage of 0.19 %. The main elements (C, O and Si) in this result were introduced by sample preparation, such as using a silicon basement for SEM imaging and glycerol for making the structure stable during drying process. All the above results demonstrate that SPIONs could adsorb on

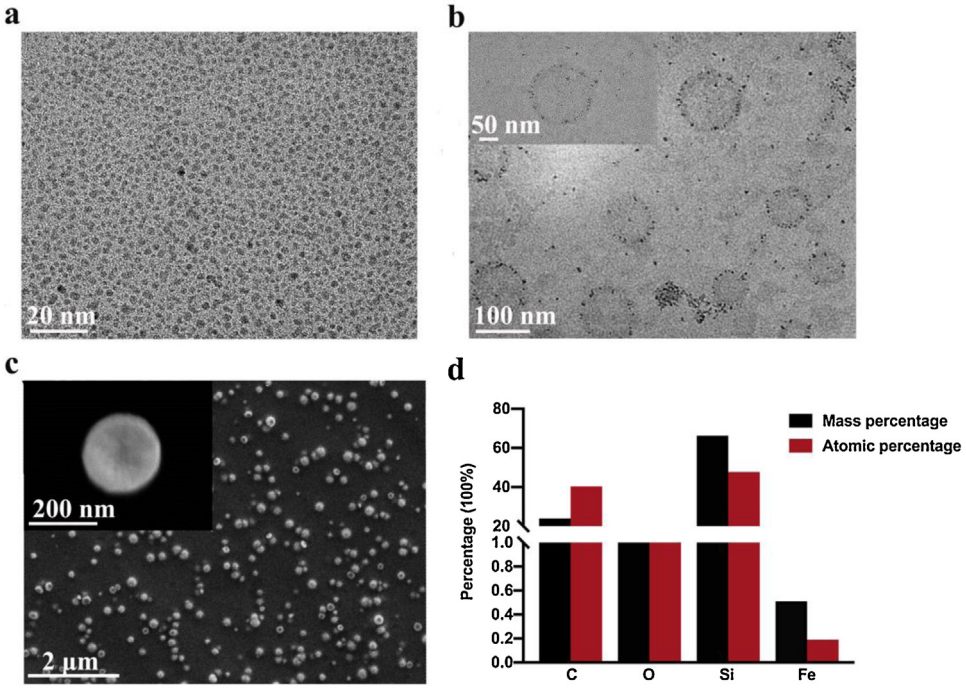

Fig. 3. Morphologies of assembled magnetic nanobubbles. (a) TEM images of SPIONs; (b) TEM images of assembled nanobubbles, and the top left corner shows the magnification of one sample; (c) SEM images of assembled nanobubbles, and the top left corner shows the magnification of one sample; (d) analysis of atomic percentage and mass percentage in assembled nanobubbles by EDS module.

the surface of nanobubbles without any polymer or phospholipid shells.

3.3. Mechanism of nanobubbles and SPIONs self-assembly

The self-assembly method of nanobubbles with SPIONs is based on cyclic compression with the change of pressure. Pushing the syringe can form a high-speed water flow in the vial, and hydrodynamic cavitation caused by the high-speed water flow causes the nanobubbles to be generated. Pulling the syringe position reduces the gas pressure in the vial, and the gas solubility is reduced, so the gas becomes supersaturated. As this time, the gas easily precipitates on the surface of the nanoparticles and in the water.

Fig. 4 shows the mechanism during the process of self-assembly of SPIONs with nanobubbles. Nanoparticles were diluted in ultrapure water, and their surface had the same electric charge. Since the nanoparticles were mutually repelled with electrostatic force, the particles were uniformly dispersed in the water and did not aggregate (Fig. 4(a)), and at this point they could all pass through the 1000 KD ultrafiltration tube, which was verified by measuring the concentration of iron (original part: 11.70 mg/L; filtered part: 11.25 mg/L). When the sample was prepared by the cyclic compression method, a gas layer was deposited on the surface of the nanoparticle (Fig. 4(b)), so there was a strong attraction between the nanoparticles with gas layer and the nanobubbles (Fig. 4(c)), and the nanoparticles then spontaneously adsorbed on the nanobubble (Fig. 4(d)). Therefore, the self-assembly of nanoparticles and nanobubbles happened in the water under the continuous pressure-driving condition. After this process was repeated numerous times, the surface of the nanobubble adsorbed dense nanoparticles. Once the nanoparticles and the nanobubbles repelled each other due to electrostatic force, the nanoparticles no longer adsorbed the nanobubbles, and the self-assembled samples stably exited in the water. The size of assembled nanobubbles was larger than free SPIONs, so the filtered part mainly became the free nanoparticles. Compared with the concentration of the original part before compression (11.07 mg/L), the filtered part was about 3.18 mg/L and the remaining part was 30.49 mg/L (some water passed through the ultrafiltration tube). The decreasing concentration of filtered SPIONs indicated the occurrence of the assembly process.

There are two key points in the method. One is to prepare a large number of nanobubbles in the water, and the other is to make the gas supersaturated in water so that the surface of nanoparticles can form a gas layer. Because of the long-range attractions, the nanobubbles and the nanoparticles with a gas layer on the surface attract each other in water to self-assemble.

The solubility of SF_6 gas in water at room temperature and room pressure is 5.40 cm^3/L. When about 10.80 μL of SF_6 is dissolved in 2 mL of water (much smaller than the volume of SF_6 used in the experiment), the effect of the pressure reduction caused by the dissolution of the gas itself can be neglected. While the piston moved to the bottom of the syringe, the volume of SF_6 changed from 5 mL to 2.00 mL. According to the ideal gas law in Eq. (1):

$$p = \frac{nRT}{V} \tag{1}$$

(p is the pressure of the ideal gas, V is the volume of the ideal gas, n is the amount of the gaseous substance, T is the thermodynamic temperature, and R is the ideal gas constant), the gas pressure increased by 2.50 times. According to Henry's Law [47,48] in Eq. (2):

$$x = \frac{P_g}{H} \tag{2}$$

where H is the Henry constant, x is the gas mole fraction solubility, and P_g is the partial pressure of the gas, the solubility of SF_6 also increased by 2.50 times. At most, 27 μL of SF_6 was dissolved in water, which was still much smaller than the volume of SF_6 used in the experiment, so the effect of the dissolution with the gas itself can be neglected too. When the piston moved to the top of the syringe, the pressure returned to normal pressure, and the SF_6 dissolved in water precipitated on the surface of the SPIONs to form

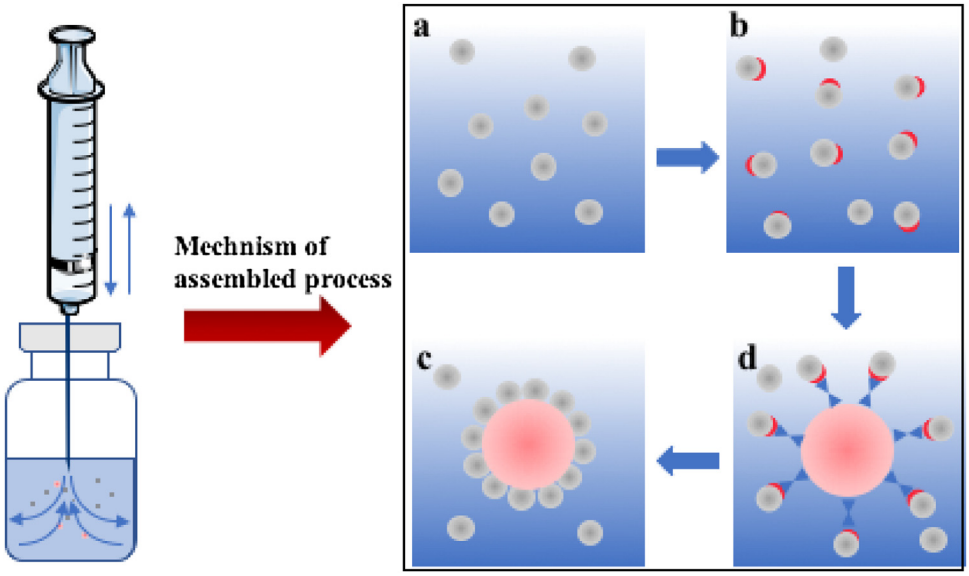

Fig. 4. Mechanism of assembled process for assembled nanobubbles. (a) SPIONs in water solution before compression; (b) a gas layer deposited on the surface of the nanoparticles during repeat compressions; (c) attractions between nanoparticles and nanobubbles; (d) the assembled nanobubbles structures.

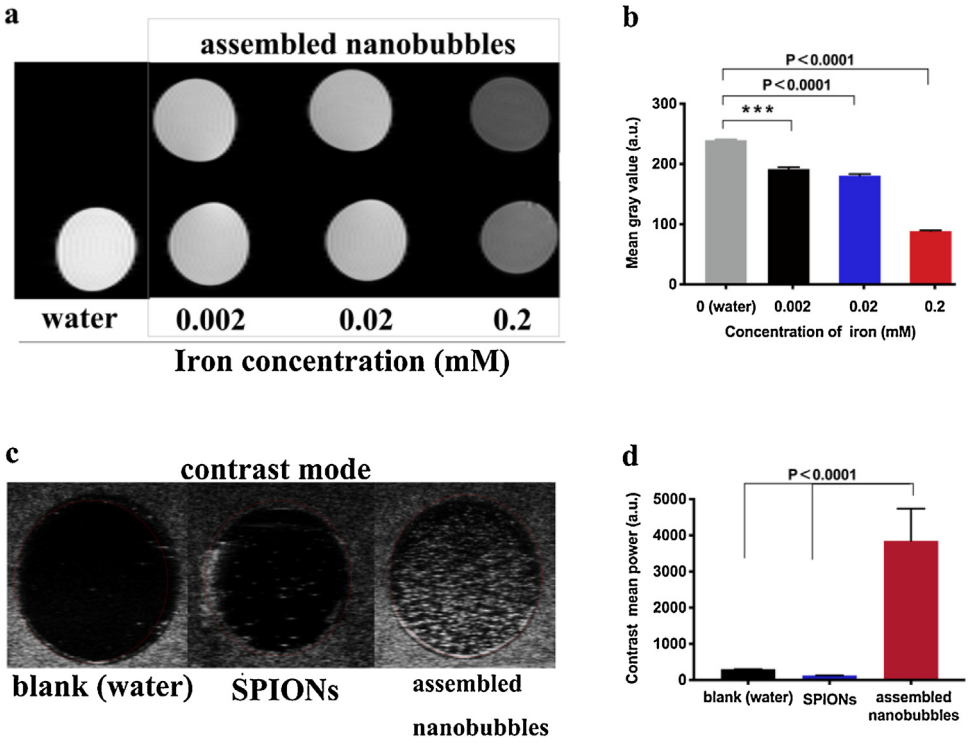

Fig. 5. MR and ultrasound imaging of assembled nanobubbles. (a) Fe concentration-dependent T_2-weighted magnetic resonance images in a 7.0 T MR scanner, and the average mean gray value of T_2 signal (b); (c) ultrasound imaging of assembled nanobubbles, and mean contrast enhanced grayscale of ultrasound imaging (d). All bars represent mean ± SD, and three independent experiments ($n = 3$) were performed; and the statistical significance is indicated by $^{***}p < 0.001$ and $^{****}p < 0.0001$.

a gas layer. At the same time, supersaturated SF_6 precipitated in water to form nanobubbles.

The velocity of fluid will become large when the fluid flows through a restricted flow zone (such as the small pipe), and that will cause the pressure in the liquid to decrease. If the pressure of liquid drops to the vapor pressure or even the negative pressure, the gas dissolved in the liquid is released to form bubbles. According to Bernoulli's Law [49] in Eq. (3), we can determine the velocity of liquid that causes the pressure in liquid to decrease to negative pressure:

$$v = \sqrt{\frac{2P_0}{\rho}} \tag{3}$$

where v is the velocity of liquid, P_0 is a constant, which is the pressure of the liquid when the velocity of liquid is 0, and ρ is the density of liquid. In the study, P_0 is the sum of gas pressure and liquid pressure, and the liquid pressure is much smaller than the gas pressure and can be ignored. When the piston is at the top of the syringe, the air pressure is equal to standard atmospheric pressure (101.30 kPa). At this time, the speed required for hydraulic cavitation is 14.21

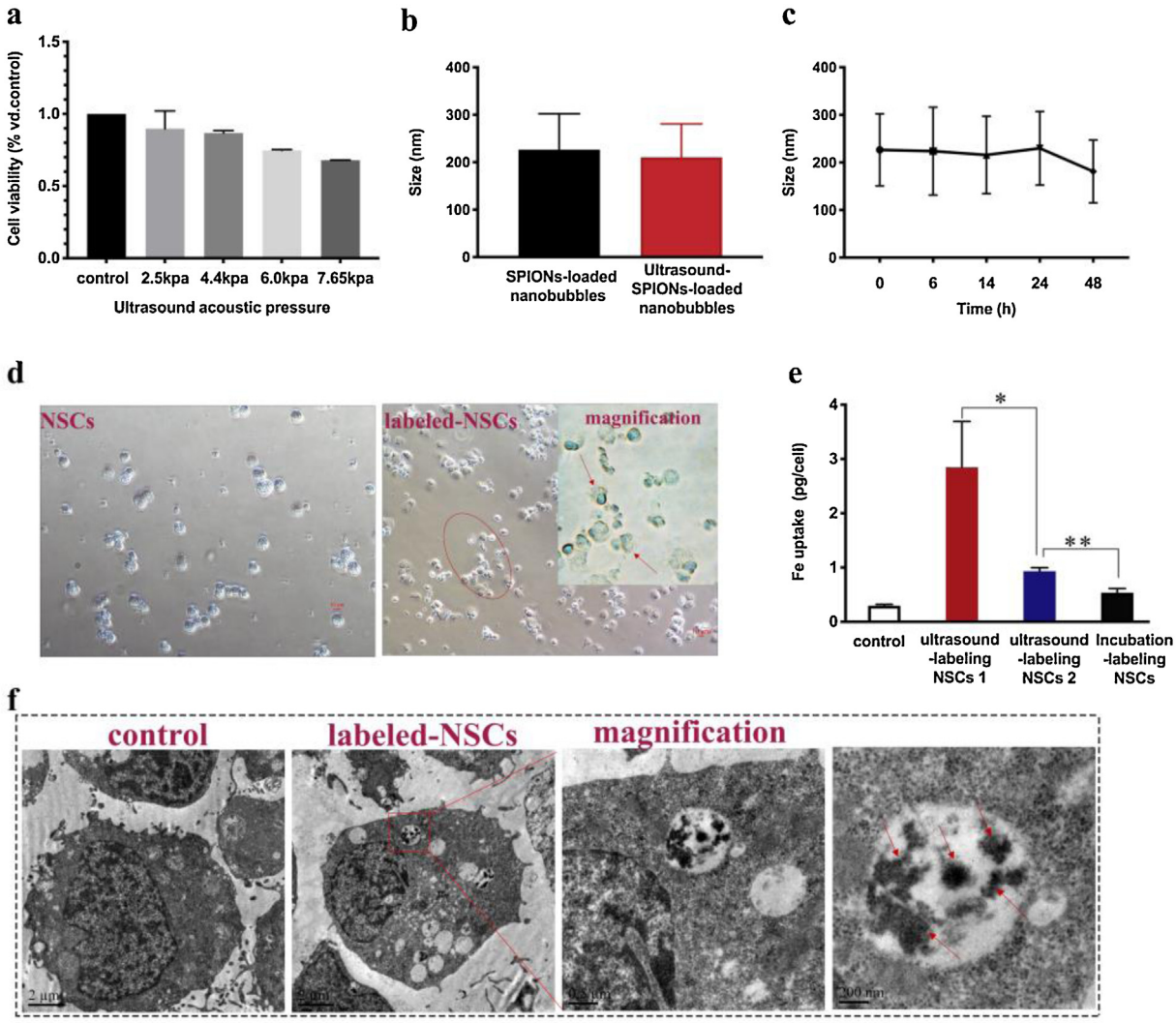

Fig. 6. Neural stem cell (NSCs) labeling in vitro. (a) Cell viability under different ultrasound acoustic pressure (2.50, 4.40, 6.00, 7.65 kPa); stability of assembled nanobubbles under ultrasound exposure (b), and in cell incubator at different time points (0, 6, 14, 24, 48 h) (c); (d) Prussian blue staining of no treatment of control cells and cells treated by nanoparticles loaded nanobubbles under the 4.40 kpa ultrasound exposure for 40 s; (e) iron concentration in one cell treated with different concentrations of iron in assembled nanobubbles or with different labeling method, and measured by ICP-OES; (f) TEM images of NSCs with and without nanoparticles loaded nanobubbles treatment. A higher-magnification image of the indicated portion is shown in the right panel. All bars represent mean ± SD, and three independent experiments ($n = 3$) were performed; and the statistical significance is indicated by $^{**}p < 0.01$ and $^{*}p < 0.05$. NSCs: Neural stem cells; SPIONs: Superparamagnetic iron oxide nanoparticles.

m/s. When the syringe piston moves to the bottom, the volume of the gas is reduced to 2/5 of the original pressure and the pressure increases to 253.25 kPa. At this time, the speed required for hydraulic cavitation is 22.50 m/s. The inner diameter of the syringe used in the experiment was 13.00 mm, and the inner diameter of the syringe needle was 0.41 mm. When the syringe piston speed was 15 mm/s, the water flow speed in the needle could exceed 14.21 m/s. When the syringe piston speed was 27 mm/s, the water flow speed in the needle could exceed 22.50 m/s.

3.4. Magnetic and acoustic performance analysis of assembled magnetic nanobubbles

To evaluate the properties of assembled nanobubbles for imaging, MR images of assembled nanobubbles were taken with a 7.0 T scanner. The T_2-weighted MR images were captured, and the mean gray value was measured by Image J (NIH, USA). The imaging result in Fig. 5(a) showed that the assembled nanobubbles with different concentrations of SPIONs, including 0.002, 0.02, and 0.20 mM, caused the T_2 signal to decrease by different amounts than the blank control of water. Meanwhile, the gray values of iron concentration at 0.20 mM and 0.02 mM showed significant difference compared to the blank control water, while the iron concentration of 0.002 mM showed significant difference (Fig. 5(b)). The higher concentration of magnetic nanobubbles indicated better MRI capabilities. These findings revealed that the assembled nanobubbles had good MRI contrast properties.

On the basis of SF_6 gas inside of bubbles, ultrasound imaging was performed on three different groups, including blank control (water), SPIONs, and assembled nanobubbles (same iron concentration with MRI: 0.20 mM). The results in Fig. 5(c, d) indicate that enhanced US imaging can be observed for the assembled nanobubbles group, and the contrast mean power showed significant differences among the three groups. The assembled nanobubbles with the concentration of 0.20 mM exhibited properties of contrast enhancement. The results of MRI contrast and ultrasound contrast property may provide assembled magnetic nanobubbles with a potential application of US/MRI dual mode imaging.

Please cite this article in press as: J. Li, et al., J. Mater. Sci. Technol. (2020), https://doi.org/10.1016/j.jmst.2020.02.045

3.5. Magnetic nanobubbles labeling the neural stem cells in vitro

Firstly, to achieve optimal ultrasound acoustic pressure, the viability of cells was measured with the CCK-8 assay. The cell suspension (with a cells: nanoparticles-loaded nanobubbles ratio of 1:10) was exposed to different acoustic pressures, including 2.50, 4.40, 6.00, and 7.65 kPa for 40 s, and NSCs without treatment were used as the control group. The result in Fig. 6(a) shows that the cells retained viability of more than 87 % at the pressures of 2.50 and 4.40 kPa after exposure. For the other two pressures, the viability decreased to 75 % and 68 %. Thus, the acoustic pressure of 4.40 kPa was used for cell labeling.

Then, the stability of the nanoparticles-loaded nanobubbles was measured with the NanoSizer to ensure their capability for cell labeling. Compared with SPIONs-loaded nanobubbles (226.60 ± 75.70 nm), the mean size of assembled nanobubbles showed no significant changes (210.40 ± 70.50 nm) (Fig. 6(b)) after ultrasound exposure. The assembled nanobubbles were also incubated for about 48 h in a cell incubator to monitor their stability, and the results showed that the size of assembled nanobubbles between 0 h (223.90 ± 77.40 nm) and 48 h (181.10 ± 66.00 nm) had no significant difference (Fig. 6(c)). All above results revealed that the assembled nanobubbles should have good stability during cell labeling studies.

To validate the feasibility of ultrasound-assisted cell labeling, Prussian blue staining was performed. As shown in Fig. 6(d), intracellular iron was stained by Prussian blue, and blue particles were seen in labeled cells (Fig. 6(d) right), whereas no blue particles were seen in the control cells without the treatment of US and assembled nanobubbles (Fig. 6(d) left). ICP-OES was further used for quantification of intracellular iron concentration to evaluate the cellular uptake. The concentration of iron in each cell was calculated according to the quantity of cells at each test point. The results show that the uptake of iron by NSCs was dependent on concentration and labeling method. It was found that there was significant difference ($p = 0.0109$) between ultrasound labeled cells 1 and ultrasound labeled cells 2 (Fig. 6(e)), and the iron uptake for these two group was about 2.84 ± 0.68 pg and 0.93 ± 0.05 pg per cell, respectively. The iron concentrations in assembled nanobubbles used in these two groups were 0.54 μg/L and 36.33 μg/L. The results indicated that the nanoparticles embedded in the nanobubbles can be delivered into stem cells, and the delivery efficiency depends on the concentration of nanoparticles loaded on nanobubbles. For further confirmation of the efficiency of the ultrasound labeling method, the incubation method (about 2 h) was applied in our study, and the iron concentration assembled on nanobubbles (36.33 μg/L) was consistent with the ultrasound labeled group. Results in Fig. 6(e) show that the iron uptake of ultrasound-labeled cells was significantly higher than incubation cells (0.54 ± 0.06 pg per cell) ($p = 0.0024$). The intracellular iron concentrations of all experimental groups were higher than the control group (cell self iron: 0.29 ± 0.02 pg per cell). To examine the internalization of materials more directly, TEM was used to visualize and confirm the endocytic structure at the ultrastructural level. Inside the labeled cells, electron-dense nanoparticles in endosomes were observed in some, but not all, endocytic vesicles, and were distributed irregularly (Fig. 6(f)). Magnetic nanobubbles were not observed on the cell membrane or in control cells (Fig. 6(f): control).

4. Conclusion

In this study, we developed a new method for self-assembly of iron oxide nanoparticles and free nanobubbles by repeated pressure-driven compression cycles. The nanoparticles can be assembled onto the nanobubble surface by simple cyclic extrusion based on the attraction of the nanobubbles to the nanoparticles with gas layers. The approach does not require any treatment of organic solvent, and the assembly of nanobubbles is simple to operate with good controllability. The assembled magnetic nanobubbles have stable structure and provide significant contrast enhancement for both US and MRI. Moreover, by utilizing the acoustic response of the assembled nanobubbles, our results reveal that the fabricated nanobubbles can be applied for neural stem cell labeling under ultrasonic exposure. Compared with the traditional co-incubation method, the magnetic nanobubble-based labeling approach indicates higher label efficiency within 40 s treatment. However, further in-depth exploration, such as studies on stem cell tracking after labeling or extension of above method for coating nanobubbles with different functional nanoparticles need to be conducted.

Acknowledgements

This investigation was financially funded by the National Key Research and Development Program of China (Nos. 2017YFA0104302, 2018YFA0704103), the National Natural Science Foundation of China (No. 81971750). And the funding partially also comes from the Natural Science Foundation of Jiangsu (No. BK20191266), the Six Talent Peaks Project of Jiangsu Province (No. 2017-SWYY-006), and Zhong Ying Young Scholar of Southeast University.

References

[1] A. Upadhyay, S.V. Dalvi, G. Gupta, N. Khanna, Mater. Sci. Eng. C 71 (2017) 425–430.
[2] N. Tabatadze, C. Tomas, R. McGonigal, B. Lin, A. Schook, A. Routtenberg, Hippocampus 22 (2012) 1228–1241.
[3] R.M. Lang, S.B. Feinstein, S.M. Powsner, C.E. McCoy, E.D. Frederickson, A. Neumann, L.I. Goldberg, K.M. Borow, Circulation 75 (1987) 229–234.
[4] S.B. Feinstein, R.M. Lang, C. Dick, A. Neumann, J. Al-Sadir, K.G. Chua, J. Carroll, T. Feldman, K.M. Borow, J. Am. Coll. Cardiol. 11 (1988) 59–65.
[5] T. Temesgen, T.T. Bui, M. Han, T.I. Kim, H. Park, Adv. Colloid Interface Sci. 246 (2017) 40–51.
[6] J. Jin, Z.Q. Feng, F. Yang, N. Gu, Langmuir 35 (2019) 4238–4245.
[7] S.H. Oh, J.M. Kim, Langmuir 33 (2017) 3818–3823.
[8] J.R. Seddon, D. Lohse, W.A. Ducker, V.S. Craig, ChemPhysChem 13 (2012) 2179–2187.
[9] A.S. Julie, E.C. Donald, C.C. Charles, S. Bhavdeep, H. Thomas, B. Howard, J. Control. Release 108 (2005) 21–32.
[10] C.L. Tang, K.J. Fang, Y.L. Guo, R. L, X.Z. Fan, P. Chen, Z.H. Chen, Q.W. Liu, Y. Zou, J. Ultrasound Med. 36 (2017) 531–538.
[11] A. Torres, S.K. Koskinen, H. Gjertsen, B. Fischler, Acta Radiol. 58 (2017) 1395–1399.
[12] R.Y. Song, C. Peng, X.N. Xu, J.W. Wang, M. Yu, Y.M. Hou, R.H. Zou, S.H. Yao, ACS Appl. Mater. Interfaces 10 (2018) 14312–14320.
[13] K. Kooiman, M.R. Bohmer, M. Emmer, H.J. Vos, C. Chlon, W.T. Shi, C.S. Hall, S.H. de Winter, K. Schroen, M. Versluis, N. de Jong, A. van Wamel, J. Control. Release 133 (2009) 109–118.
[14] S.H. Bloch, M. Wan, P.A. Dayton, K.W. Ferrara, Appl. Phys. Lett. 84 (2004) 631–633.
[15] M. Gauthier, Q. Yin, J.J. Cheng, W.D. O'Brien, J. Ultrasound Med. 34 (2015) 1363–1372.
[16] W. He, F. Yang, Y.H. Wu, S. Wen, P. Chen, Y. Zhang, N. Gu, Mater. Lett. 68 (2012) 64–67.
[17] T.A. Rovers, G. Sala, E. van der Linden, M.B. Meinders, ACS Appl. Mater. Interfaces 8 (2016) 333–340.
[18] D. Vlaskou, O. Mykhaylyk, F. Krötz, N. Hellwig, R. Renner, U. Schillinger, B. Gleich, A. Heidsieck, G. Schmitz, K. Hensel, C. Plank, Adv. Funct. Mater. 20 (2010) 3881–3894.
[19] O. Mykhaylyk, Y. Sanchez-Antequera, D. Vlaskou, M.B. Cerda, M. Bokharaei, E. Hammerschmid, M. Anton, C. Plank, Methods Mol. Biol. 1218 (2015) 53–106.
[20] H. Chen, J. Li, W.Z. Zhou, E.G. Pelan, S.D. Stoyanov, L.N. Arnaudov, H.A. Stone, Langmuir 30 (2014) 4262–4266.
[21] T.B. Brismar, D. Grishenkov, B. Gustafsson, J. Harmark, A. Barrefelt, S.V. Kothapalli, S. Margheritelli, L. Oddo, K. Caidahl, H. Hebert, G. Paradossi, Biomacromolecules 13 (2012) 1390–1399.
[22] G.M. Whitesides, Nature 442 (2006) 368–373.
[23] H. Kanaka, T. Esra, L.L. Marjorie, A.D. Paul, P.L. Abraham, Lab Chip 7 (2007) 463–468.
[24] J. Owen, C. Crake, J.Y. Lee, D. Carugo, E. Beguin, A.A. Khrapitchev, R.J. Browning, N. Sibson, E.A. Stride, Drug Deliv. Transl. Res. 8 (2018) 342–356.

[25] M. Chinol, P. Casalini, M. Maggiolo, S. Canevari, E.S. Omodeo, P. Caliceti, F.M. Veronese, M. Cremonesi, F. Chiolerio, E. Nardone, A.G. Siccardi, G. Paganelli, Br. J. Cancer 78 (1998) 189–197.
[26] F. Yang, Y.X. Li, Z.P. Chen, Y. Zhang, J.R. Wu, N. Gu, Biomaterials 30 (2009) 3882–3890.
[27] L. Duan, F. Yang, L.N. Song, K. Fang, J.L. Tian, Y.J. Liang, M.X. Li, N. Xu, Z.D. Chen, Y. Zhang, N. Gu, Soft Matter 11 (2015) 5492–5500.
[28] J.I. Park, D. Jagadeesan, R. Williams, W. Oakden, S. Chung, G.J. Stanisz, E. Kumacheva, ACS Nano 4 (2010) 6579–6586.
[29] T. Lammers, P. Koczera, S. Fokong, F. Gremse, J. Ehling, M. Vogt, A. Pich, G. Storm, M. van Zandvoort, F. Kiessling, Adv. Funct. Mater. 25 (2015) 36–43.
[30] H. Mulvana, R.J. Eckersley, M.X. Tang, Q. Pankhurst, E. Stride, Ultrasound Med. Biol. 38 (2012) 864–875.
[31] E. Stride, C. Porter, A.G. Prieto, Q. Pankhurst, Ultrasound Med. Biol. 35 (2009) 861–868.
[32] B.H. Luo, H.J. Zhang, X.H. Liu, R. Rao, Y. Wu, W. Liu, Biomed. Mater. Eng. 26 (Suppl. 1) (2015) S911–S916.
[33] N.T.K. Thanh, L.A.W. Green, Nano Today 5 (2010) 213–230.
[34] W. Cai, X. Chen, Small 3 (2007) 1840–1854.
[35] C.R. Bjornson, R.L. Rietze, B.A. Reynolds, M.C. Magli, A.L. Vescovi, Science 283 (1999) 534–537.
[36] J.D. Bernstock, L. Peruzzotti-Jametti, D. Ye, F.A. Gessler, D. Maric, N. Vicario, Y.J. Lee, S. Pluchino, J.M. Hallenbeck, J. Cereb, Blood Flow Metab. 37 (2017) 2314–2319.
[37] M. Stenudd, H. Sabelstrom, J. Frisen, JAMA Neurol. 72 (2015) 235–237.
[38] M. Yousefifard, V. Rahimi-Movaghar, F. Nasirinezhad, M. Baikpour, S. Safari, S. Saadat, A. Moghadas Jafari, H. Asady, S.M. Razavi Tousi, M. Hosseini, Neuroscience 322 (2016) 377–397.
[39] W.J. Cui, S. Tavri, M.J. Benchimol, M. Itani, E.S. Olson, H. Zhang, M. Decyk, R.G. Ramirez, C.V. Barback, Y. Kono, R.F. Mattrey, Biomaterials 34 (2013) 4926–4935.
[40] L. Gong, C.Q. Jiang, L. Liu, S.X. Wan, W. Tan, S.S. Ma, X.J. Jia, M.W. Wang, A. Hu, Y. Shi, Y. Zhang, Y.Y. Shen, F. Wang, Y. Chen, Exp. Ther. Med. 15 (2018) 620–626.
[41] Y.Q. Wang, C.J. Xu, H. Ow, Theranostics 3 (2013) 544–560.
[42] H.L. Lei, X. Nan, Z.Y. Wang, L. Gao, L.S. Xie, C. Zou, Q. Wan, D. Pan, N. Beauchamp, X.M. Yang, T. Matula, B.S. Qiu, J. Nanosci. Nanotechnol. 15 (2015) 2605–2612.
[43] L.J. Arnold JR., A. Dagan, J. Gutheil, N.O. Kaplan, Proc. Natl. Acad. Sci. U. S. A. 76 (1979) 3246–3250.
[44] B. Chen, J.F. Sun, F.G. Fan, X.Z. Zhang, Z.G. Qin, P. Wang, Y. Li, X.Q. Zhang, F. Liu, Y.L. Liu, M. Ji, N. Gu, Nanoscale 10 (2018) 7369–7376.
[45] G.L. Zhang, L.K. Chen, W.H. Chen, B.Q. Li, Y.B. Yu, F. Lin, X.Y. Guo, H. Wang, G.J. Wu, B. Gu, W. Miao, J. Kong, X.X. Jin, G.Q. Yi, Y. You, X.H. Su, N. Gu, J. Biomed. Nanotechnol. 14 (2018) 1178–1188.
[46] F. Yang, M.X. Li, H.T. Cui, T.T. Wang, Z.W. Chen, L.N. Song, Z.X. Gu, Y. Zhang, N. Gu, Sci. China Mater. 58 (2015) 467–480.
[47] C.A. Ward, E. Levart, J. Appl. Phys. 56 (1984) 491–500.
[48] D.M. Avishay, K.M. Tenny, Henry's Law, StatPearls Publishing books in 2019, 2019.
[49] K.H. Støverud, H.P. Langtangen, V. Haughton, K.A. Mardal, Neuroradiol. J. 26 (2013) 218–226.

Please cite this article in press as: J. Li, et al., J. Mater. Sci. Technol. (2020), https://doi.org/10.1016/j.jmst.2020.02.045